Journal of The Electrochemical Society, **161** (10) A1706-A1715 (2014)
0013-4651/2014/161(10)/A1706/10/$31.00 © The Electrochemical Society

Solvent-Coupled Catalysis of the Oxygen Electrode Reactions in Lithium-Air Batteries

Matthew J. Trahan,[a,*] Iromie Gunasekara,[a,*] Sanjeev Mukerjee,[a,] Edward J. Plichta,[b] Mary A. Hendrickson,[b] and K. M. Abraham[a,**,z]**

[a]*Department of Chemistry and Chemical Biology, Northeastern University, Boston, Massachusetts 02115, USA*
[b]*Power Division, US Army RDECOM CERDEC CP&I, RDER-CCP, Aberdeen Proving Ground, Maryland 21005, USA*

The electrocatalysis of oxygen reduction reactions (ORR) in non-aqueous electrolytes is coupled to the ability of the solvents to modulate the Lewis acidity of Li^+. This is accomplished through chemical interactions of Li^+ with the solvent to form acid-base complexes of the general formula, $Li(solvent)_n^+$, which determine the relative stability of the ORR intermediates and the final products formed. In high Donor Number solvents such as dimethyl sulfoxide (DMSO), the ORR proceeds via an outer Helmholtz plane (OHP) reaction pathway, conforming to a homogeneous catalysis of the reaction, irrespective of the presence of a catalyst in the cathode. In low Donor Number solvents exemplified by tetraethylene glycol dimethyl ether (TEGDME) and CH_3CN, catalysts such as cobalt phthalocyanine (CoPC), Pt and Au promote heterogeneous electrocatalysis at the inner Helmholtz plane (IHP) of the electrical double layer on the electrode. The catalysis in this case involve the adsorption of O_2 as well as the ORR intermediates on the catalyst surface leading to lower activation energy of the reactions and increases in the discharge voltages of Li-air cells compared to uncatalyzed cells. The heterogeneous catalysis at the IHP may promote the full electrochemical reduction of O_2 to O^{2-}.
 [DOI: 10.1149/2.0981410jes]

Manuscript submitted April 14, 2014; revised manuscript received June 23, 2014. Published July 29, 2014.

Recent investigations[1–4] of oxygen reduction reactions (ORR) in non-aqueous electrolytes for Li-air batteries have revealed that the ion-conducting salt cations and the organic solvents play important roles on the ORR mechanism and the stability of the ORR products formed. This dominant coupling of ORR to the nature of the electrolyte has been explained using the Hard Soft Acid Base (HSAB) concept which states that hard Lewis acid ions want to combine with hard Lewis bases while soft Lewis acids like to be associated with soft Lewis bases.[2,5,6] The relevance of the HSAB concept to ORR in non-aqueous electrolytes is that the Lewis acid properties of the electrolyte salt cations are modulated by their solvation (or acid-base complex formation) with the solvents, which lead to strong correlations between the ORR mechanism and the solvent's Lewis basicity. Solvents with high Guttmann Donor Numbers (DN) are strong Lewis bases which make Li^+ cations softer Lewis acids through the formation of solvates of the type, $Li^+(solvent)_n$. Depending on the DN of the solvents used to prepare the non-aqueous electrolytes, the Li^+ cation acquires a range of hard-soft Lewis acidities which in turn controls the mechanism and products of ORR. In this communication, we wish to report that the ORR catalysis activity in non-aqueous electrolytes is coupled to the Lewis basicity of the solvent as measured by its donor number (DN).[6] This makes the ORR process in non-aqueous electrolytes unique and different from that generally observed in aqueous electrolytes in which the nature of the solvent (H_2O) remains invariant with the presence of the strongest Lewis acid cation, H^+. In aqueous electrolytes the ORR pathway and the stability of the ORR intermediate are influenced by the pH scale and it has been found that the peroxide intermediate is more prevalent as the pH increases.[7,8] Recognition of the variable Lewis acidity of Li^+ in non-aqueous electrolytes is vital to the development of appropriate catalysts for the non-aqueous Li-air battery for which the choice of electrolytes is potentially large. While we acknowledge the many recent studies demonstrating the influence of catalysts on the discharge reactions and rechargeability of the Li-air battery[9–38] the present work using the CoPC-based catalyst suggests that the knowledge gained from fuel cell catalysis may be insufficient to explain the ORR pathways and products formed in non-aqueous Li-air batteries. The data presented in this communication will show that ORR catalysis can proceed via either a homogeneous (outer Helmholtz plane reaction) or a heterogeneous (inner Helmholtz plane reaction) pathway. This information is expected to satisfactorily explain and unify the results of the various ORR catalysis studies pertaining to non-aqueous Li-air batteries.

Experimental

Catalyst preparation.— Cobalt catalyst powder samples were prepared as previously described.[39] Briefly cobalt phthalocyanine (CoPC) was dissolved in a concentrated sulfuric acid solution after which high surface carbon (either Vulcan XC72R for thin film studies or Ketjen300 for full cell studies) was added under stirring until a homogenous paste was formulated. The quantity of carbon black added was fixed to achieve a 2 wt% Co concentration of the solid phase components. The paste was then instantaneously diluted via directly transferring into a large volume of deionized water forcing CoPC to precipitate out of solution and deposit onto the carbon black. The carbon black/CoPC particulate suspension was then separated via vacuum filtration and the resulting powder was dried under vacuum at 70°C. Dried powder samples were then loaded into an argon purged quartz tube and sintered in a furnace at either 600°C or 800°C for four hours.

The two catalyzed carbons thus prepared are designated as Co600 and Co800. Uncatalyzed Vulcan carbon samples were also prepared via the same procedure described above. The resulting carbon powder products were analyzed by powder X-ray diffraction using a Rigaku Ultima IV Bragg-Brentano para-focusing diffractometer with a Cu k_α radiation source. The identity of the catalyst on the carbon was established by X-ray absorption spectroscopy (XAS) measurements collected in transmission mode at the Co K-edge at beam line X-3A at the National Synchrotron Light Source (NSLS) at Brookhaven National Laboratory. All the experimental XAS data were processed utilizing the IFEFFIT suite version 1.2.11. Each datum is calibrated to the same energy scale by carefully aligning each scan of a cobalt reference foil which had been collected simultaneously during each sample scan. The XAS data was analyzed using Athena and Artemis programs.[40]

Voltammetric measurements.— High surface area carbon ink suspensions for thin film electrodes for voltammetry experiments were created by dissolving a polyvinylidene fluoride (PVDF) (Kynar 2801) binder material into a N-methyl-2-pyrrolidone solvent, and then adding the catalyzed or uncatalyzed carbon powder (90:10 powder: binder by mass) to the binder solution and sonicating until a homogenous ink suspension resulted. Microliter aliquots of the ink suspension were cured onto a 0.196 cm^2 glassy carbon change tip disk working electrode (from Pine Instrument Company) at 80°C under vacuum creating carbon/catalyst films of 100 micro gram (μg) cm^{-2} on the

*Electrochemical Society Student Member.
**Electrochemical Society Fellow.
zE-mail: kmabraham@comcast.net

disk electrode. Additional experiments were conducted with both a platinum and gold change tip disk electrode of the same diameter.

All electrochemical experiments were carried out in the absence of air and moisture in an Argon-filled MBraun Labmaster 130 glove box maintained with a moisture level of below 1 ppm. Purolyte lithium hexafluorophosphate ($LiPF_6$) certified to contain less than 20.0 ppm water was purchased from Novolyte Technologies and used as received. Metals basis 99.9% Li foil was used as received from Alfa Aesar company. Upon receipt from the vendor, all these reagents were immediately stored in the argon-filled glove box. Electrolyte formulations were carried out in the dry atmosphere glove box using class B polypropylene volumetric flasks and an APX 153 top loading balance from Denver Instruments.

The test cells for electrochemical experiments were airtight and were handled using techniques employed in the manipulation of air-sensitive compounds. Anhydrous grade $\geq$ 99.8% acetonitrile (CH_3CN), purum grade $\geq$98.0% tetraethylene glycol dimethyl ether (TEGDME), and anhydrous grade DMSO certified to contain less than 50 ppm water, were purchased from Sigma Aldrich and stored in the dry atmosphere glove box upon receipt. The rest of the 1–2% of materials in TEGDME was composed of other glyme ethers with similar chemical properties as TEGDME. For some experiments the solvents were dried with 0.3–0.4 nm activated molecular sieves and the water contents of the dried solvents were checked using the Karl-Fisher titration method. The drying procedures for the various solvents have been described previously in publications dealing with ORR in the corresponding electrolytes.[4–6] The electrochemistry did not show any impact from this final drying.

Cyclic voltammetry experiments were conducted utilizing a PG-STAT30 bipotentiastat equipped with a scangen module from Ecochemie Inc. Electrolytes were prepared in the glove box using polypropylene class B volumetric flasks. A polypropylene screw cap container from Nalgene was employed as the cell container and an in-house fabricated polypropylene lid was in place to keep the electrolyte solution removed from the ambient room conditions and to hold the electrodes in a stationary fashion, as described previously.[5,6] Oxygen gas was purged into the cell through a solvent reservoir in order to solvate the gas flow thereby minimizing the evaporation of the electrolyte solvent. Platinum gauze was utilized as the counter electrode, the working electrode prepared as described above, and an in house assembled reference electrode made from a silver wire contained in a 100 mM $TBAPF_6$, 10 mM silver nitrate acetonitrile solution in a glass tube, was used. For the DMSO and TEGDME based electrolytes, the Li/Li^+ scale were directly measured by monitoring the potential of the reference electrode from an actual lithium ribbon submerged in the electrolyte solution.

For the CH_3CN-based electrolyte, the reference cell was routinely calibrated in separate cyclic voltammetry experiments conducted in tenth molar $TBAPF_6$ acetonitrile electrolytes with the addition of 1 mM Ferrocene. Steady state scans collected at 50 mVs^{-1} with a planar glassy carbon disk working electrode, were utilized to determine the potential of the reference cell from the ferrocene/ferrocenium couple. The silver reference cell couple was consistently found to be approximately 88 mV below the formal reduction potential of the standard ferrocene/ferrocenium couple. The data plots shown here in are shifted to the Li/Li^+ scale after measuring the potential of the ferrocene/ferrocenium versus a Li foil immersed in the electrolyte.

Rotating ring disk electrode (RRDE).— The ring-disk electrode consists of two electrically insulated electrodes, one a glassy carbon disk of 0.247 cm^2, the other a gold ring of 0.187 cm^2, located immediately outside the disk circumference. For the rotating electrode experiments, the ring electrode was held at a constant potential from the Ag/Ag^+ reference electrode. This potential value was determined separately for each electrolyte by measuring the voltammetric response of a gold electrode in the oxygenated electrolyte to determine a potential where superoxide was expected to be oxidized in the voltage window of the electrolyte.

Fabrication of Li/O_2 cell cathodes.— Powder dispersions were formulated in N-methyl-2-pyrolidinone solutions containing already dissolved Kynar 2801 binder material. The powder to binder ratio of these inks was fixed at 90:10 by mass. The inks were delivered via pipette to one inch diameter precut Panex conductive carbon cloth substrates and cured under vacuum at 80°C. Typical mass loadings were between 2–4 mg cm^{-2}.

Li/O_2 Cell assembly and characterization procedures.— All assembly procedures were carried out in an MBraun Labmaster 130 Argon dry atmosphere glove box with H_2O vapor levels maintained below 1 ppm. The cathodes were saturated with electrolyte under vacuum in the glove box's antechamber at approximately 1 bar below atmosphere. A 32 mm diameter lithium foil disk was cut with a steel die from a 1.5 mm thick ribbon as received from Alfa Aesar. A 50 mesh copper current collector was pressed into the lithium foil between two polypropylene sheets. The copper current collector was screwed into the stainless steel electrode terminal via a stainless steel bolt and nut mounting hardware. A circular cut out of a microporous polypropylene membrane separator was placed on top of the anode. The cathode was then removed from the antechamber vacuum and placed onto a paper Kimwipe, drained of excess electrolyte, massed (approximately 150–200 mg of electrolyte per cathode), and placed on top of the polypropylene membrane with the high surface area carbon material faced inward to the lithium foil. An aluminum Dexmet cut out was placed on top of the cathode to supply a uniform compressing force between the electrode areas and allow for current collection through the cathode cell terminal. Galvanostatic charge/discharge cycling of the cells was performed on an Arbin Instruments BT2000 model cycler.

Results and Discussion

Influence of donor number on superoxide stability.— Non-aqueous electrolytes are composed of Li salts dissolved in solvents having a range of electron donor properties (basicities) defined by the Gutmann Donor Number (DN). The DN is the enthalpy of reaction in kcal/mole for the reaction between the solvent and antimony pentachloride chloride ($SbCl_5$) in dichloroethane (CH_2ClCH_2Cl).[41] The higher the DN of the solvent, the stronger is its tendency to donate electrons (i.e., Lewis basicity) to form electron-donor complexes with Lewis acids such as Li^+. Recently, we have shown[2] from ^{13}C NMR chemical shift and spin-lattice relaxation time (T1) data that the Li^+ ions in Li salt solutions in non-aqueous electrolytes are solvated, typically by four solvent molecules per Li^+, to form the complexes or solvates, $Li\text{-}(solvent)_4{}^+$. The formation of these solvates lowers the acidity hardness of Li^+ making it a softer Lewis acid in proportion to the degree of electron donation by the solvent. In other words, the higher the DN of the solvent, the softer the solvated Li^+ becomes. We can obtain a reasonable quantitative measure of this softening of Li^+ Lewis acidity from the solvation energy for the reaction between the solvent and Li^+, determined using the formula in equation 1, developed by Drago et al.[42]

$$-\Delta H = E_A E_B + C_A C_B + R_A T_B \qquad [1]$$

In equation 1, ΔH is the enthalpy (in kcal/mole) of formation of a Lewis acid-base adduct, E_A, C_A and R_A are parameters characteristic of the acid, and E_B, C_B and T_B are parameters characteristic of the base. These parameters for Li^+ and some of the solvents used in non-aqueous Li batteries, CH_3CN, $(CH_3)_2SO$ and $(C_2H_5)_2O$, are listed in Table I. These parameters for Li^+ are $E_A = 11.72$, $C_A = 1.45$ and $R_A = 24.21$ and those for $(CH_3)_2SO$ are $E_B = 2.4$, $C_B = 1.47$, and $T_B = 0.65$ all values in kcal/mole.[42] The enthalpy of formation calculated for a 1:1 adduct between Li^+ and DMSO is about 46 kcal/mole whereas that for Li^+ and CH_3CN is approximately 40 kcal/mole.[43] A similar trend should follow for adducts formed between a Li^+ and four solvent molecules. Since the solvent parameters for TEGDME are not known we have calculated the solvation energy for the solvate formed between Li^+ and diethyl ether as a representative of ether solvates.

Table I. Acid and Base parameters for Li^+ and some non-aqueous solvents (CH_3CN, $(C_2H_5)_2O$, $(CH_3)_2SO$), and the Enthalpy of formation ($-\Delta H$) calculated for a 1:1 adduct between Li^+ and the solvent.

Acid	E_A	C_A	R_A	Base	DN	E_B	C_B	T_B	$-\Delta H$ / kcal mol^{-1}
Li^+	11.72	1.45	24.21	CH_3CN	14.1	1.64	0.71	0.83	40.32
				$(C_2H_5)_2O$	19.2	1.80	1.63	0.76	41.85
				$(CH_3)_2SO$	29.8	2.40	1.47	0.65	45.82

Clearly, the higher solvation energy involved in the formation of the complex $Li^+(DMSO)_n$ translates into lower Lewis acidity for the Li^+ in DMSO than for Li^+ in CH_3CN and diethyl ether. The higher solvation energy calculated for the solvate formed between DMSO and Li^+ is consistent with that expected from its high Donor Number of 29.8 compared with a donor number of 14.1 for CH_3CN and 19.2 for diethyl ether. These data provide theoretical support for the HSAB concept to explain the ORR mechanism and the products formed in electrolytes prepared with these solvents. The correlation observed in Table I between the enthalpies of formation for the 1:1 adducts of Li^+ and the solvents and their Donor Numbers provide a relative measure of the softening of the acidity hardness of Li^+ by the solvent. Clearly, these data lend support to the view that solvated Li^+ in DMSO is a softer Lewis acid than the solvated Li^+ present in CH_3CN and in the ethers.

The generally recognized ORR reactions in non-aqueous electrolytes are depicted in equations 2–4.[2–6] In the high donor number solvent DMSO, the one-electron ORR product, superoxide (O_2^-), (equation 2) is stabilized in solution with longer lifetimes whereas in low donor solvents such as acetonitrile (CH_3CN, DN = 14.1) and tetraethylene glycol dimethyl ether (TEGDME; DN = 16), the superoxide has shorter life times and quickly decomposes into the stable two-electron reduction product, peroxide (O_2^{2-}), in an overall two-electron reaction (sum of equations 2 and 3). The peroxide can also be formed by further electrochemical reduction of the superoxide as depicted in equation 4.

$$O_2 + e^- + Li^+ \rightarrow LiO_2 \quad [2]$$

$$LiO_2 \rightarrow 1/2Li_2O_2 + 1/2O_2 \quad [3]$$

$$LiO_2 + e^- + Li^+ \rightarrow Li_2O_2 \quad [4]$$

This ability of the solvents to stabilize different ORR products in Li^+-conducting electrolytes has been explained on the basis of the Hard-Soft-Acid-Base (HSAB) concept.[2–6,44]

Our ORR results on catalyzed electrodes in non-aqueous electrolytes have revealed that there is a striking influence of the solvents' DN (or basicity) on the ORR catalysis process. We have found that ORR on carbon electrodes in electrolytes based on high DN solvents prefers to take place in the outer Helmholtz plane of the electrical double layer (outer plane ORR) regardless of the presence of a catalyst, whereas in electrolytes utilizing low DN solvents, the ORR on a catalyzed electrode is facilitated in the inner Helmholtz plane of the electrical double layer (inner plane ORR), making the ORR process both catalyst and solvent dependent in non-aqueous electrolytes. In the absence of a catalyst in low DN solvent-based electrolytes such as $LiPF_6$ in TEGDME, an outer plane ORR is seen as well, although the superoxide formed in the first electron transfer to O_2 is less stabilized through ion-pair formation in solution by the $Li^+(TEGDME)_n$ solvate (as $Li^+(TEGDME)_n$–O_2^-), since it is a harder Lewis acid. The superoxide quickly decomposes to peroxide (equation 3) as the overall oxygen reduction product. Experimental support for these observations is provided below.

Effect of catalyst surfaces on ORR in low electron donor solvent-based electrolytes.— A way to differentiate the inner Helmholtz plane (IHP) ORR process from the outer Helmholtz plane (OHP) process is by careful analysis of the voltammetric response from four different working electrode surfaces in oxygenated electrolytes in both low and high donor number solvent-based electrolytes. Some properties of the electrolytes used in this study are given in Table II.

Table II. Properties of solvents and their Li salt solutions.

0.1M $LiPF_6$ in	Solvent Donor Number /kcal mol^{-1}	Conductivity /mS cm^{-1}	O_2 Solubility /mM
DMSO	29.8[a]	2.11[c]	2.1[d]
TEGDME	16.6[b]	0.3[c]	4.43[e]
CH_3CN	14.1[a]	14.39[c]	8.1[d]

[a]Gutmann;[41]
[b]Mamantov;[47]
[c]Ó'laoire[48]
[d]Sawyer et. al.;[49]
[e]Zhang et. al.[50]

The catalysts used in this study include Pt, Au and the two materials derived from CoPC. The Pt and Au were disk electrodes while the CoPC derived catalysts in carbon powder were used as thin films on a glassy carbon disk. We recently reported the detailed characterization of the Co-600 catalyst using X-ray absorption spectroscopy (XAS).[45] In the Co-600 carbon catalyst powder, the CoPC chemical structure (Scheme 1) mostly remains intact. During the sintering at 600°C, CoPC acquires an amorphous morphology with some loss of hydrogen in the process of chemically attaching itself to the carbon black. A comparison of the X-ray Absorption Near Edge Spectra (XANES) for the as-received CoPC material, the Co600 material, as well as three cobalt standard materials (having a cobalt oxidation state of zero, two, and three) is presented in Figure 1.

Specifically, the edge peak feature, a spectroscopic signature of the planar Co-N_4 geometry, which peaks at 7716 eV remains intact after pyrolysis at 600°C confirming that the thermal treatment is mild enough to avoid degradation of the macrocycle. The Co-800 catalyst shows the XANES signature for Co metal. This was confirmed by the XRD patterns measured from the Co600 and Co800 powder samples

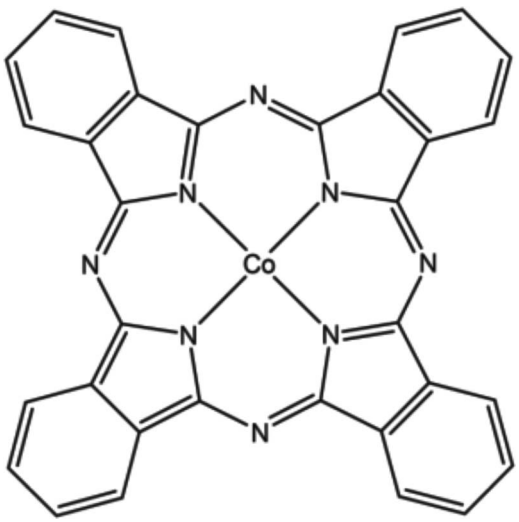

Scheme 1. Molecular structure of Cobalt (II) phthalocyanine.

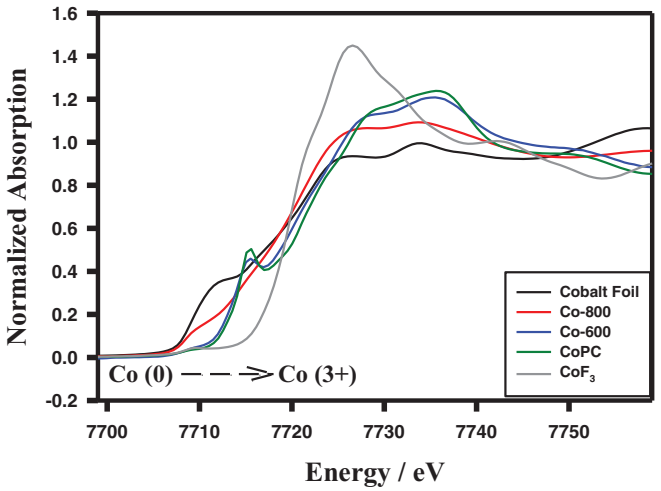

Figure 1. Overlay of XANES spectra from Cobalt metal foil, Co-800, Co-600, CoPC, and CoF_3. The arrow indicates the shift to higher ionization energy as the cobalt atom's oxidation state increases.

given in Figure 2. There is a metallic cobalt signal present in the powder which was processed at 800°C while this feature is absent in the pattern of the sample processed at 600°C which further confirms that the macrocycle remains intact in the CoN_4 configuration at the lower temperature. The Co-800 catalyst was characterized from both XAS and XRD data to be composed of highly divided cobalt metal in the carbon matrix.

For the cyclic voltammetry experiments in Figures 3 and 4, the solvent is CH_3CN, a low Donor Number solvent. The disk working electrodes utilized were the noble metals gold and platinum, and vitreous carbon. One important difference in the voltammograms on these three disk electrodes is found in the current response measured just prior to the onset of the faradaic ORR process. This region of the voltammogram is expanded in Figure 3a. At approximately 2.9 V, there is a distinguished pre-peak feature present in the current response of the noble metal electrodes in contrast to the carbon disk which has no such pre-peak feature. This region is highlighted with a yellow ellipse. The charge associated with the pre-peaks on catalyzed electrodes is estimated to be in the microcoulombs/cm^2 range as expected for adsorption peaks.

We interpret this pre-peak feature in the reductive wave to be associated with the direct adsorption of the oxygen from the outer

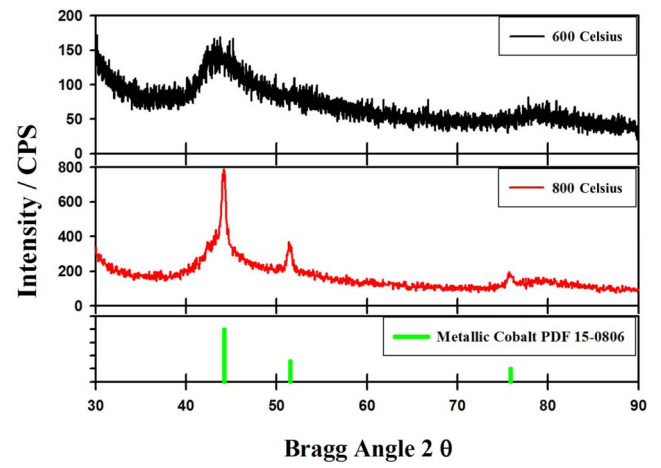

Figure 2. X-ray diffraction pattern measured from the CoPC on Vulcan carbon powder samples heat treated at 600°C and 800°C. The lowest plot shows the database pattern corresponding to metallic cobalt.

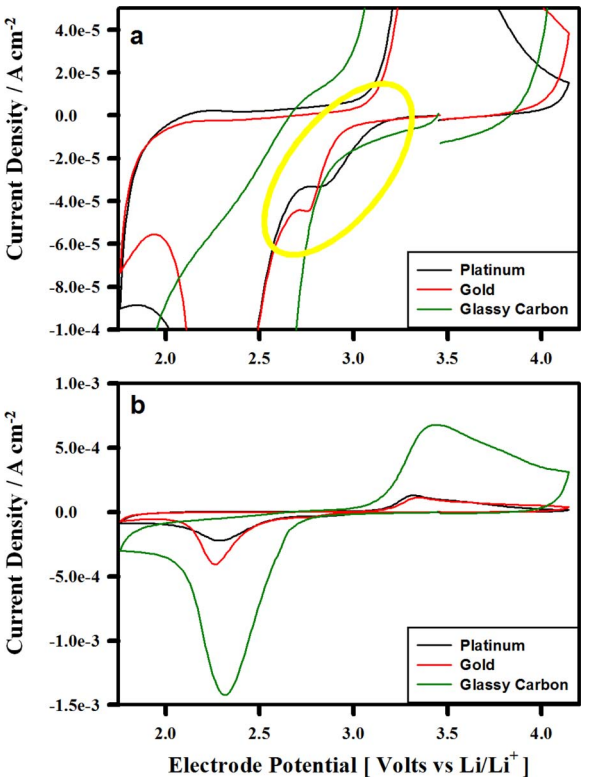

Figure 3. First sweep voltammograms measured at 100 mV s^{-1} in oxygenated 0.1 M $LiPF_6$ in CH_3CN with three separate working electrode disks over the potential range of 1.5 to 4.0 V versus Li/Li^+. (a) plotted at a current range of 0.05 mA cm^{-2} to 0.1 mA cm^{-2} and (b) plotted at a current range of 1 mA cm^{-2} to −1.5 mA cm^{-2}.

Helmholtz plane to the inner Helmholtz plane of the double layer onto the noble metal surfaces. This feature is not seen in the catalyst-free carbon surface indicating that the charge transfer in this case probably proceeds via an outer plane electron transfer at the carbon/electrolyte interface. The O_2 adsorption on the noble metals is facilitated by their electronic structures which provide energetically favorable adsorption sites that are not present on the surface of the carbon electrode. Similar features in the voltammograms of noble metal electrodes have been observed in low donor solvent-based electrolytes previously (Figure 5)[12] although the implication of that finding was not discussed. One consequence of this adsorption is apparent in Figure 3b where the reduction peak currents for the three electrodes are compared. Clearly, the two noble metal surfaces, which facilitate the direct adsorption of the oxygen at the inner Helmholtz plane prior to reduction, experience more severe passivation than the carbon electrode as evident by the peak current magnitudes. This can be explained by the notion that at the inner Helmholtz plane, charge transfer process would result in the deposition of the ORR product more tightly bound to the electrode surface and therefore more effectively passivate the electrode interface than an outer Helmholtz plane process. This is supported further by the comparison of the platinum electrode response with that of gold. The platinum pre-peak feature starts at lower over-potential than on gold, and, consequently, shows more peak current suppression than on gold. This shift in adsorption onset has been predicted by DFT calculations of the metal-oxygen bond energy for platinum (4.2 eV) compared to gold (2.7 eV)[46] and it is telling that the oxygen is more closely bound (shorter bond distance) to the platinum surface than it is to gold. Therefore, the change in free energy for the adsorption on platinum is more effective in lowering the activation energy for the overall charge transfer process. This trend further affirms that the pre-edge current signal does in fact correspond to an oxygen adsorption to the metal surface.

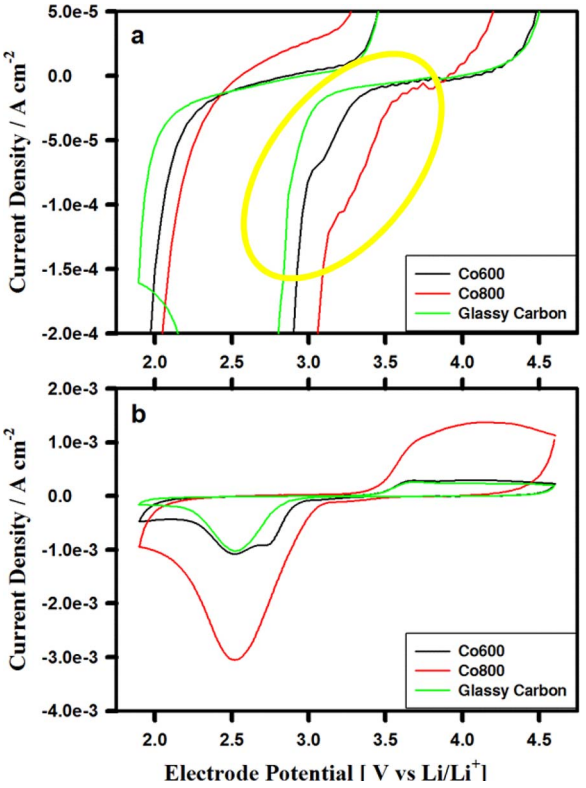

Figure 4. First sweep voltammograms measured at 100 mV s^{-1} in oxygenated 0.1 M $LiPF_6$ CH_3CN with three separate working electrode surfaces scanned between 2 and 4.5 V versus Li/Li^+. (a) Plotted at a current range of 0.05 mA cm^{-2} to −0.2 mA cm^{-2} and (b) plotted at a current range of −4 mA cm^{-2} to 2.0 mA cm^{-2}.

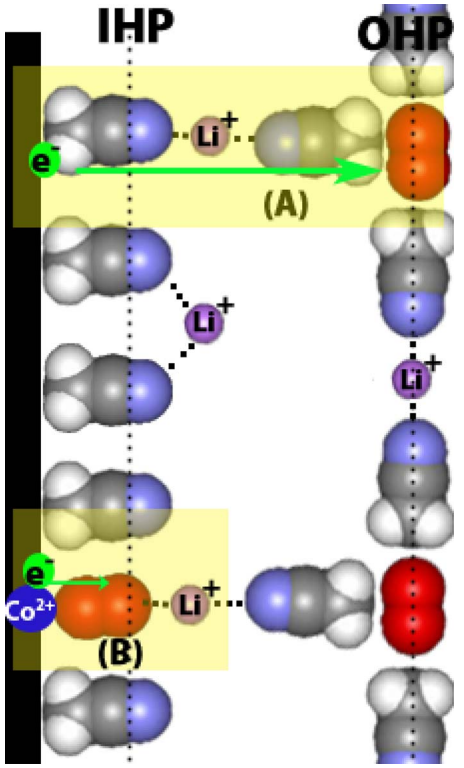

Figure 5. A schematic representation of the electrochemical double layer at the interface of a Co600 catalyzed carbon electrode in a Li^+-$(CH_3CN)_n$ electrolyte. Highlighted section A shows the outer Helmholtz plane one electron charge transfer as it occurs on an uncatalyzed surface. Highlighted section B shows inner Helmholtz plane charge transfer process facilitated by the presence of a catalyzed surface.

In addition to the gold and platinum surfaces, there also is a pre-peak feature in the current response of the cobalt phthalocyanine catalyzed high surface carbon black electrode which we studied under the same conditions. As shown in Figure 4a for ORR in 0.1 M $LiPF_6$ /CH_3CN, the CV on both the Co800 and the Co600 displays a pre-peak adsorption signature prior to the onset of faradaic current flow which is comparable to that measured from the noble metal electrodes shown in Figure 3a. For these high surface area carbon catalyst-containing films, the pre-edge feature is not as sharply defined as it was for the noble metal disks shown in Figure 3a, probably due to the film surface being comprised of a mixture of both carbon surface and cobalt catalyst surfaces. The data in Figure 4b indicate that the presence of the Co800 (metallic cobalt) material in the high surface area carbon network causes a 400 mV positive shift in the onset of the ORR. This shift is a result of the lowering of the activation energy for the superoxide product formation. The electronic configurations of the superoxide (O_2^-), CoPC, and the Co metal surface are shown below in Scheme 2. Both Co metal and Co^{2+} have empty electron orbitals to enable adsorption of O_2 and its reduction products.

In the low donor number CH_3CN solvent-based electrolyte, the gold, platinum, cobalt metal, and cobalt-N_4 (Co600) electrode surfaces appear to lower the activation energy for ORR by facilitating oxygen adsorption and stabilization of the ORR product intermediate through a direct surface adsorption. A graphical display of this proposed difference between outer (region A) and inner (region B) Helmholtz plane electron transfer processes is shown in the Schematic in Figure 5 for the possible double layer structure in low Donor Number solvent-based electrolytes.

Effect of catalyst surfaces on ORR in high electron donor solvent-based electrolytes.— These same electrodes exhibited little effect on the ORR potentials in the electrolyte based on the high Donor Number DMSO solvent. In this high DN electrolyte, an outer Helmholtz plane homogenous catalysis appears to stabilize the ORR intermediate and product regardless of the presence of catalyst in the electrode as discussed below.

The observed influence of the solvent DN on the ORR mechanism and products can be understood by considering the change in the electrode double layer structure of the same working electrodes in DMSO-based electrolytes. Figure 6a shows an expansion of the same current range displayed in the CH_3CN voltammograms of Figure 3a for the same three disk electrodes now in the DMSO-based electrolyte.

In contrast to the voltammograms measured in CH_3CN-based electrolytes, neither of the noble metal electrodes nor the vitreous carbon electrode shows any pre-peak response in the DMSO/$LiPF_6$ solution. The unique feature in this electrolyte is the current peak at 2.5 V (in

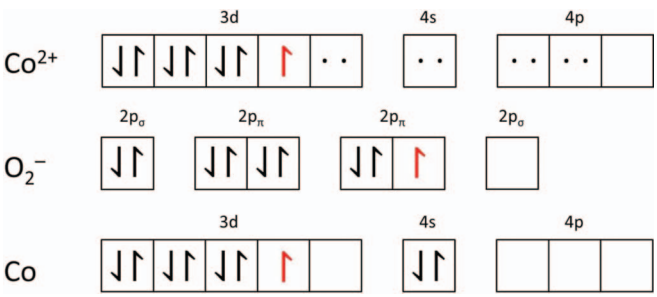

Scheme 2. Electronic Structure diagram of the superoxide intermediate, Co^{2+} and metallic cobalt. Electrons native to the Co^{2+} are represented by arrows whereas the electrons shared with the nitrogen ligands to form CoPC are represented by dots. Unpaired electrons are highlighted by the red font.

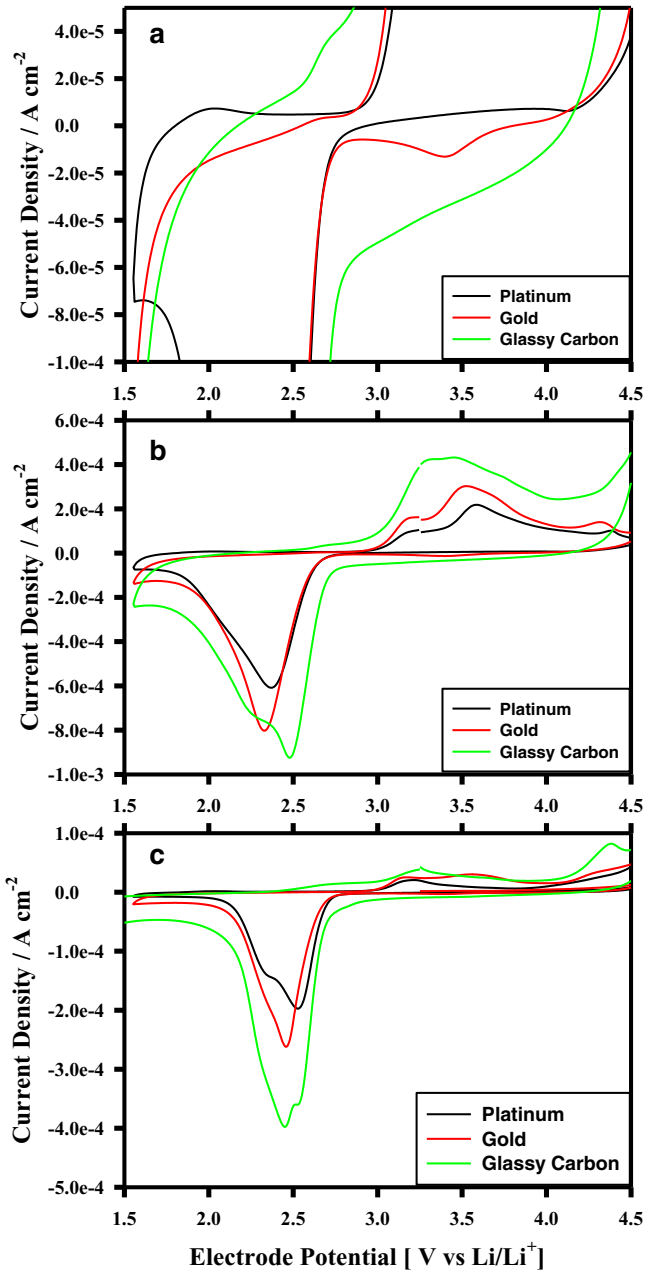

Figure 6. Third sweep voltammograms measured at 100 mV s^{-1} in oxygenated 0.1 M $LiPF_6$ in DMSO with three separate working electrode disks; plotted at a current range of (a) −0.1 mA cm^{-2} to 0.05 mA cm^{-2} and (b) −1.0 mA cm^{-2} to 0.6 mA cm^{-2} (c) voltammograms measured at 10 mV s^{-1}.

Figures 6b and 6c) on the glassy carbon electrode, assigned to the formation of the one-electron reduction product superoxide (O_2^-) which is stable in this electrolyte as we have already reported.[4] The superoxide reduction intermediate is stabilized by the softer acid $Li^+(DMSO)_n$ solvate through the formation of the ion pair $Li^+(DMSO)_n$—O_2^-. The charge transfer in this case most probably proceeds via an outer Helmholtz plane pathway (outer plane process), and it dominates the ORR pathway irrespective of whether or not a catalysts is present on the electrode surface. A visual description of this homogenous catalysis is depicted in Figure 7 (part A displays the outer plane electron transfer) which shows the schematic of the double layer interface structure in the high DN-based Li^+-electrolyte.

Because of the dominance of the high donor number DMSO medium in promoting the outer plane ORR process, there is no additional increase in the ORR voltage due to the CoPC catalyst in this electrolyte. However, a close examination of the results in Figures 3 and Figure 6 indicate that the nature of the catalyst has a secondary role on ORR in high donor number solvents. First of all, the limiting ORR peak currents measured on Pt, Au and vitreous carbon in the DMSO medium are much closer in magnitude than those observed in the CH_3CN electrolyte. This indicates that the electrode passivation is occurring more rapidly in the CH_3CN based electrolyte, especially for the noble metal surfaces, as a result of the direct adsorption of the oxygen to the metal surface. For the DMSO-based electrolyte the three disk electrodes have nearly identical onset potentials for ORR and the noble metals do not appear to be facilitating catalysis of the first step in the reduction process. Further understanding of the differences caused by the chemistry of the disk material can be gained by analysis of the reduction wave measured at slower sweep rates. Figure 6c shows the response of the three electrodes at 10 mV s^{-1} allowing direct comparison of the relative peak current magnitudes of the first and second waves in the ORR process for the three electrode materials. As a reminder, the first peak in the diffusion controlled process corresponds to the one electron reduction of oxygen to superoxide.[4] The broad shoulder observable upon further cathodic over-potential corresponds to the further electrochemical reduction of the superoxide to form insoluble materials which lead to disk passivation. Some noteworthy observations regarding Figures 6b and 6c is that the carbon disk shows this distinguished broad peak even at the faster sweep rate (Figure 6b) while this feature is not as pronounced on the noble metal electrodes unless slower sweep rates are utilized. Furthermore, the slower sweep rate voltammogram for the carbon disk actually shows a greater peak current for the second cathodic process. These observations suggest that the superoxide formed initially in the OHP has a greater propensity to adsorb to the noble metal surfaces than to the carbon surface resulting in two effects. According to this model, first, the superoxide is stabilized on the noble metal inhibiting

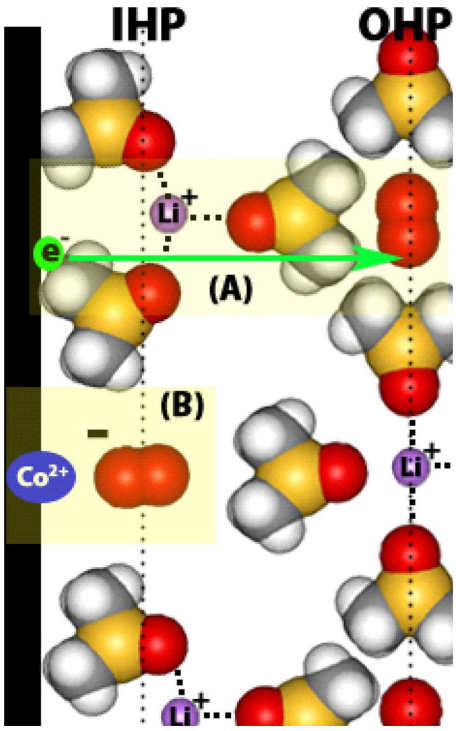

Figure 7. A schematic representation of the electrochemical double layer at the interface of a Co600 catalyzed carbon electrode and a Li^+-DMSO electrolyte. Highlighted section A shows the outer Helmholtz plane one electron charge transfer. Highlighted section B shows the one electron product superoxide chemisorbed to the Cobalt catalyst in the inner Helmholtz plane promoting further electrochemical reduction of the oxygen radical.

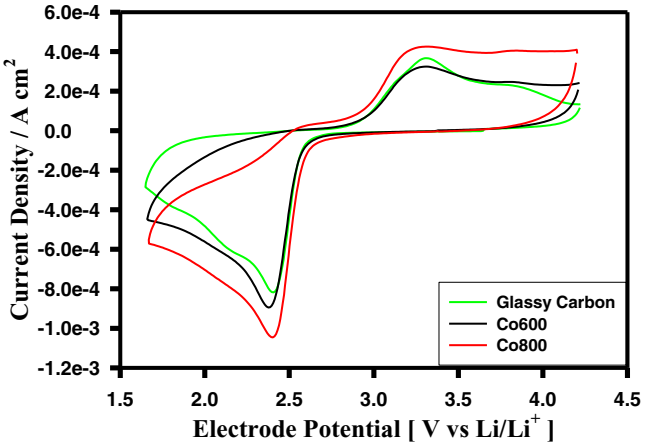

Figure 8. First sweep voltammograms measured at 100 mV s^{-1} in oxygenated 0.1 M $LiPF_6$ in DMSO with three separate working electrode surfaces.

possible side reactions with solvent molecules. Secondly, the direct adsorption of the O_2^- intermediate promotes its further reduction to O_2^{2-} and to O^{2-}.

Additionally, the CVs of cobalt-catalyzed carbon electrodes were also measured in the DMSO electrolyte as shown in Figure 8. These voltammograms indicate that neither the Co800 nor the Co600 electrode is effective at lowering the overpotential required for oxygen reduction beyond that of DMSO itself on the vitreous carbon electrode. These various results in DMSO are consistent with the notion that the Li^+-containing electrolyte in DMSO functions as a homogenous catalyst through an outer Helmholtz plane ORR process by stabilizing the one-electron ORR intermediate superoxide by forming ion-pairs with solvated Li^+, i.e; $Li^+(DMSO)_n$—O_2^-. The stabilization of the superoxide ORR product in high donor number DMSO-based Li^+ electrolytes supersedes the adsorption of oxygen by the cobalt catalysts with the result that a homogeneous outer layer (OHP) catalysis path persists in these electrolytes. Note that we have identified both O_2^{2-} and O^{2-} in Li-air cells with CoPC (Co600) catalyzed electrodes.[45] The superoxide intermediate adsorption is shown schematically in region B of Figure 7 for a CoPC-based catalyst. On the other hand, the vitreous carbon electrode surface does not have the electronic feature to adsorb the superoxide (O_2^-) to the electrode and therefore it remains solvated in the OHP where it can either undergo chemical decomposition to Li_2O_2 or take part in possible side reactions with the solvent.

Rotating ring disk experiments to assess inner or outer helmholtz plane reaction.— Evidence for the electrolyte's role in facilitating the outer or inner Helmholtz layer ORR charge transfer process can be gathered by measuring the current response from the ring electrode of a rotating ring disk electrode assembly in electrolytes prepared in different solvents. In this technique, materials which are generated at the working electrode interface can be detected if they are released into the bulk electrolyte and transported to the ring electrode. As shown in Figure 9 there is a strong correlation between the solvent donor number in Li^+-electrolytes and the quantity of solution-stabilized superoxide ORR intermediate generated at the disk.

Clearly, the ring response measured in the DMSO-based electrolyte is significantly larger than that measured in the TEGDME-based electrolyte. This effect is further quantified by plotting the integrated charge area corresponding to the ring's oxidation process (after collection efficiency adjustment) normalized by the integrated charge area corresponding to the disc's reductive wave as a function of Donor Number as shown in Figure 9c. This finding emphasizes that the superoxide intermediate is not long-lived in the low DN solvent-based electrolytes as it is prone to undergo rapid chemical reaction with the harder acid Li^+ to produce Li_2O_2. For these low DN solvent-based

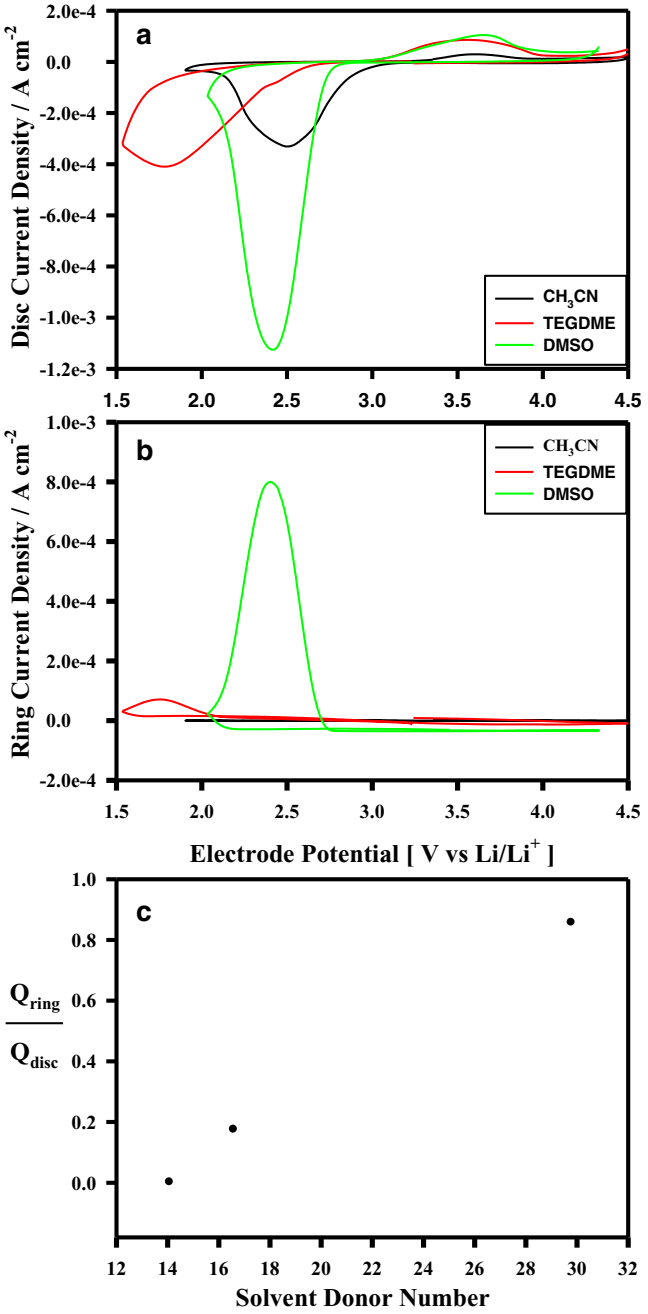

Figure 9. RRDE response of a glassy carbon disk measured in three aprotic Li^+-electrolytes of varying donor number. (a) Disk response (b) Ring response (c) charge ratio as a function of donor number. The ring electrode is biased to 3.6 V, 3.2 V, 2.9 V vs Li/Li$^+$ for the CH_3CN, TEGDME, DMSO experiments, respectively.

electrolytes the presence of a heterogeneous electrode catalyst can effectively lower the activation energy required to reach full reduction of oxygen by stabilizing the intermediate and therefore providing an advantage in cell voltage and coulombic capacity.

The RRDE voltammetry was also applied to the same cobalt catalyzed high surface area films discussed above in the DMSO electrolyte and their response is shown in Figure 10. Again, there is no advantage in the ORR onset for either of the two catalyst films as compared to the uncoated planar disk in this high DN electrolyte. Interestingly, small changes in the ring current response (both in regards to peak magnitude and onset potential) can be detected as shown in Figure 10b. The glassy carbon working electrode shows the greatest

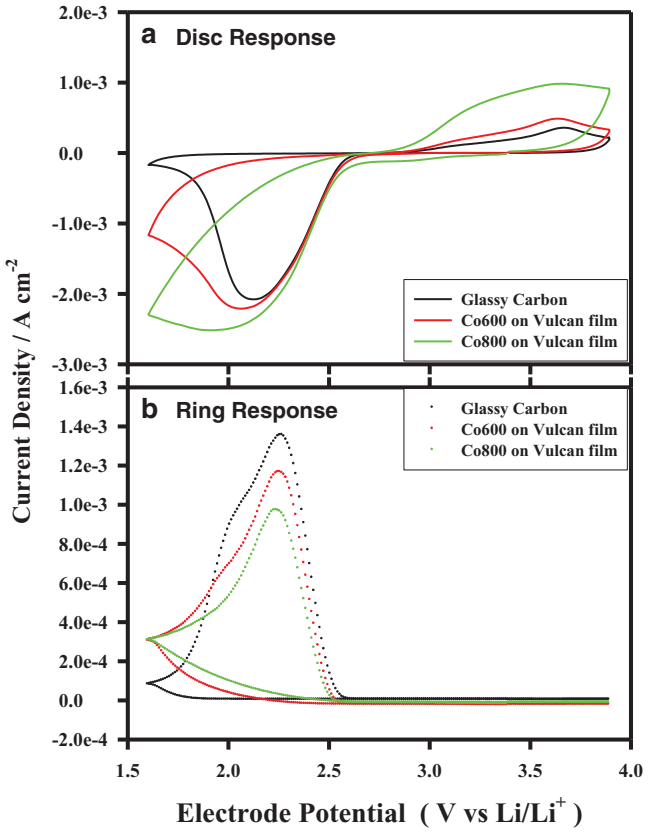

Figure 10. RRDE response collected at 500 rpm from three separate working electrode surfaces measured at 100 mV s^{-1} in oxygenated 0.1 M $LiPF_6$ in DMSO. (a) Shows the disk response (b) shows the response of the gold ring while biased at 2.93 V vs Li/Li^+.

peak in ring current response and also the earliest onset of oxidative current flow, followed by the Co600 film and then the Co800 film which has the lowest ring current peak magnitude and the latest onset of the oxidative current flow. We interpret this trend to be indicative of an increase in the rate at which the superoxide reduction product is further reduced electrochemically as it passes along the working electrode interface on the way to the ring electrode. We have included a visual description of this process in the Figure 7 B schematic of the high DN electrolyte double layer. This second charge transfer process also explains the slight increase in the limiting current measured at the disk in the following order Glassy Carbon< Co600 < Co800. The same trend in the ring response (both in regard to the magnitude and also the time delay) was observed in the TEGDME-based electrolyte as shown in Figure 11.

The magnitude of the superoxide detection at the ring electrode from the Co800 film is less than half of that detected from the planar carbon disk (albeit after larger limiting current magnitudes from the film), again suggesting that the superoxide intermediate is more prone to be reduced further as it travels along the Co800 electrode interface than it does in the case of the Co600 or the planar carbon electrode. The observed shifts in onset of ring current flow are much larger in the TEGDME-based electrolyte than those observed in the DMSO-based electrolyte. For the former electrolyte the ring current response is nearly an order of magnitude lower than those measured in the DMSO-based electrolyte. Both of these observations support the prolonged stability of the superoxide in the DMSO-based Li^+ electrolyte; and support the preponderance of the outer Helmholtz plane process in high DN solvent-based electrolytes.

Cobalt-Catalyzed Li-air cell performance of the high and low donor number based-electrolytes.— In order to provide further support to the homogeneous catalysis and the stability of the ORR intermediate O_2^- in electrolytes based on high donor number solvents, we have studied the discharge behavior of Li/O_2 cells filled with DMSO-1M $LiPF_6$ electrolyte and both catalyzed and uncatalyzed carbon cathodes. Shown in Figure 12 is an overlay of the discharge curves for both the uncatalyzed Ketjen300 and the Co600 catalyzed Ketjen black electrodes assembled with DMSO-based cells. Although, the voltage of the catalyzed cell is initially higher for a brief duration (see inset Figure 12), the catalyzed cell quickly steps down to the same voltage plateau as the uncatalyzed cathode for the remaining cell discharge capacity.

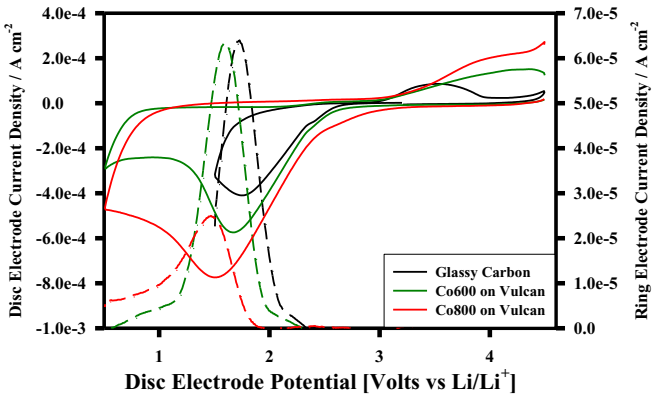

Figure 11. RRDE response collected at 500 rpm from three separate working electrode surfaces measured at 100 mV s^{-1} in oxygenated 0.1 M $LiPF_6$ in TEGDME. The disk response is plotted in solid line style on the left hand current scale while the ring response is in dashed line style on the right hand current scale.

The discharge voltage of cells assembled with the low DN solvent TEGDME is markedly different from that of the cells with DMSO. As shown in Figure 13, we observed that the Co600 catalyzed electrodes discharge at about 200 mV higher than the uncatalyzed Ketjen300 electrode in this low DN electrolyte. The discharge products in this electrolyte included Li_2O_2 and Li_2O (we have recently reported the details of the product analysis from Co600 catalyzed electrodes).[45] These observations are consistent with our half-cell voltammetry results which support the view that high DN solvents supersede the advantage of having a catalyzed cathode material. As we reported recently, based on the various analytical data presented in this paper and those obtained previously[45] the overall ORR reactions on

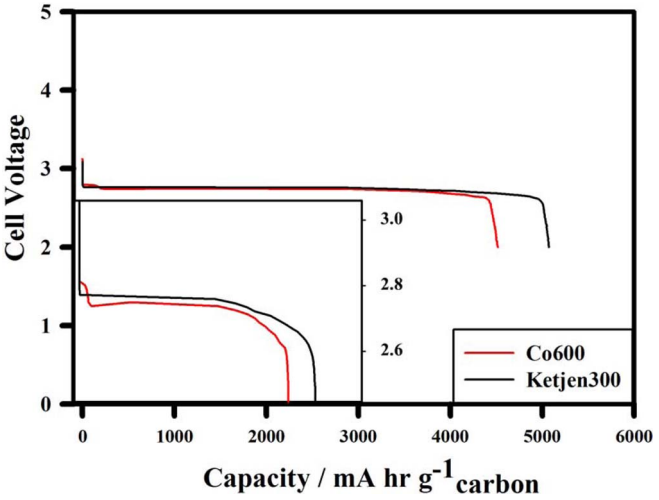

Figure 12. Galvanostatic Discharge of a Co600 catalyzed Ketjen cathode and an uncatalyzed Ketjen cathode measured in 1M $LiPF_6$ in DMSO at a current density of 0.1 mA cm^{-2}. Inset shows an expansion of the voltage range from 2.5 to 3.0 Volts.

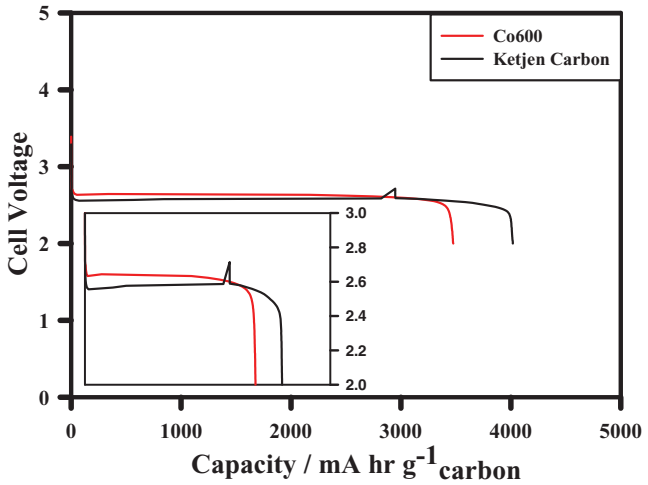

Figure 13. Galvanostatic Discharge of a Co600 catalyzed Ketjen black cathode and an uncatalyzed Ketjen black cathode measured in 1M $LiPF_6$ in TEGDME at a rate of 0.1 mA cm^{-2}. Inset shows an expansion of the voltage range from 2.0 to 3.0 Volts.

Co600 catalyzed electrodes in the low DN solvent-based electrolyte TEGDME/$LiPF_6$ are those depicted in equations 5–8

$$Co600 + O_2 \rightarrow Co600 - O_2 \quad [5]$$

$$Co600 - O_2 + e^- + Li^+ \rightarrow Co600 - O_2^- Li^+ \quad [6]$$

$$2\,Co600 - O_2^- Li^+ \rightarrow Co600 - O_2Li_2 + O_2 \quad [7]$$

$$Co600 - O_2Li_2 + 2Li^+ + 2e^- \rightarrow 2Li_2O + Co600 \quad [8]$$

Both Li_2O_2 (with characteristic d-values of 2.720, 2.568 and 1.565 Å in its X-ray diffraction pattern) and Li_2O (with d-value in its diffraction pattern at 2.703 Å characteristic of the major peak for Li_2O) have been identified as discharge products of the cells using Co600 catalyst. A Li-air cell discharged with a Ketjen black electrode containing the Co800 catalysts showed about a 200 mV higher load voltage than the uncatalyzed cell. However, only Li_2O_2 was identified as the discharge product from the carbon cathode of this cell. Figure 14 shows continuous cycling of the Li-O_2 cells with both Co800 catalyzed (a) and uncatalyzed (b) carbon electrodes. The Co800 catalyzed cell showed improved cycle performance and the discharge voltage plateau remained unchanged until the 20th cycle.

It appears that while the unpaired electrons on the Co metal in Co800 promote the adsorption of O_2 to facilitate an inner Helmholtz plane reaction in TEGDME, the absorption of the reduction product peroxide, O_2^{2-}, appears to be weak on this surface to promote the full four-electron reduction of O_2 to O^{2-}.

The formation of Li_2O product in Li-air cell cathodes catalyzed by Co600 suggests that for the adsorption of the peroxide O_2^{2-} and its reduction to O^{2-}, the Co-N_4 moiety present in the Co600 catalyst is required. The in situ XANES data we previously obtained[44] for the ORR process on the Co600 catalyst were consistent with the end-on adsorption of O_2 to the catalyst surface prior to the formation of O_2^-. Figure 15a displays this end-on adsorption of the oxygen molecule to the Co metal center in a CoPC molecule. End-on absorption of O_2 on to the Co metal catalyst in Co800 is also possible and the formation of Li_2O_2 as the final discharge product in Co800-catalyzed cells is consistent with this view. For the catalyzed reduction of Li_2O_2 to Li_2O the side-on adsorption of peroxide (O_2^{2-}) to the catalyst surface is the most favored configuration because of the presence of two negative charges on the peroxide molecule. A side-on adsorption of the peroxide to the Co600 catalyst is reasonable since the oxygen farther away from the Co^{2+} center can interact with one of the nitrogen atoms in the -N_4- moiety having a partial positive charge resulting

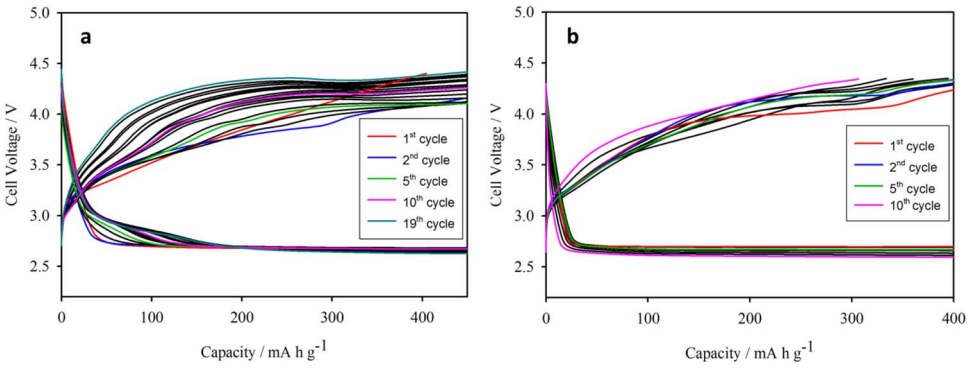

Figure 14. Li-O_2 cell cycling in 1M Li^+/TEGDME at a discharge rate of 0.1 mA cm^{-2}. a) Co800 catalyzed, b) Ketjen black catalyzed cells.

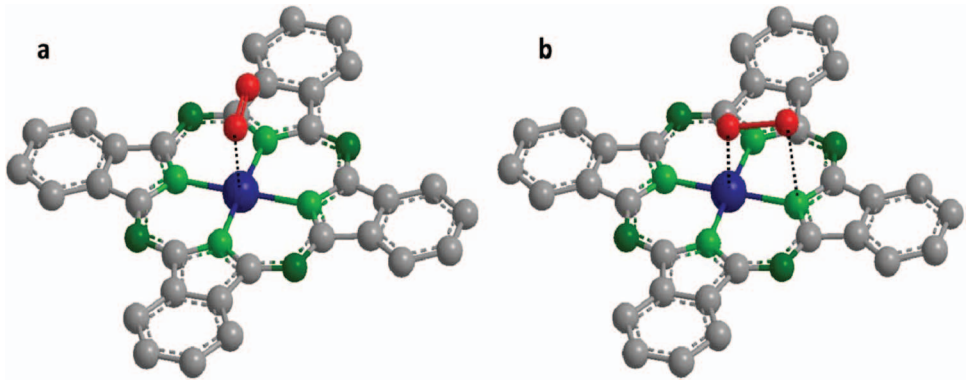

Figure 15. Co-N_4 facilitated Oxygen reduction reaction by Co600 Catalyst, a) end-on adsorption of the Oxygen molecule on the Co center in the macrocycle, b) side-on interaction of the peroxide molecule with the Co-N_4 moiety.

from electron delocalization on the macrocycle. Thus the $Co^{2+}N_4^{\delta-}$ entity facilitates a side-on adsorption of the peroxide ion as shown in Figure 15b and promotes the reduction of the peroxide to monoxide as depicted in equation 8. The -N_4- moiety in conjunction with Co^{2+} required for the side-on adsorption is not present in the Co800 catalyst and as result the O_2 reduction reaction is terminated at the peroxide stage on the Co800 catalyst.

Conclusions

Cyclic and ring-disk voltammetry data obtained in this work have revealed that oxygen reduction reactions on vitreous carbon electrodes occur via an outer Helmholtz plane (OHP) mechanism. The Donor Number or the basicity of the electrolyte solvent plays a dominant role on the stability of the initial one electron O_2 reduction product, O_2^-, and hence the mechanism of the reaction. In electrolytes based on high donor solvents such as DMSO, the O_2^- is stabilized by the formation of stable ion pairs of the type $Li^+(DMSO)_n—O_2^-$ between solvated Li^+ and O_2^-. As a result the activation energy for electron transfer is lowered to provide a higher voltage for the Li-air cells utilizing DMSO-based electrolytes Thus, high donor number solvents homogeneously catalyze oxygen reduction reaction. The homogeneous catalysis of the high donor number solvent is so dominant that cathode catalysts such as CoPC showed little ORR catalytic activity in DMSO-based electrolytes. In the absence of a catalyst in the carbon cathode in low DN solvent-based electrolytes such as CH_3CN and TEGDME, there appears to be no homogeneous catalysis despite an outer Helmholtz layer OHP) ORR process. In these low DN solvent-based electrolytes, catalysts such as CoPC, Pt and Au promote an inner Helmholtz plane (IHP) ORR process due to the strong adsorption of O_2 as well as the ORR intermediates O_2^- and O_2^{2-} on to the catalyst surface with the result that a four-electron reduction of O_2 to O^{2-} occurs in these electrolyte. The adsorption of these intermediate reduction products on the catalyst surface may lower the propensity for these materials to react with the solvents leading to improved stability for the Li-air battery.

Acknowledgments

We sincerely thank U.S. Army CERDEC for the financial support provided through subcontract No. GTS-S-13–025 for this work.

References

1. K. M. Abraham and Z. Jiang, *Journal of The Electrochemical Society*, **143**, 1 (1996).
2. C. J. Allen, J. Hwang, R. Kautz, S. Mukerjee, E. J. Plichta, M. A. Hendrickson, and K. M. Abraham, *The Journal of Physical Chemistry C*, **116**, 20755 (2012).
3. C. J. Allen, S. Mukerjee, E. J. Plichta, M. A. Hendrickson, and K. M. Abraham, *The Journal of Physical Chemistry Letters*, **2**, 2420 (2011).
4. M. J. Trahan, S. Mukerjee, E. J. Plichta, M. A. Hendrickson, and K. M. Abraham, *Journal of The Electrochemical Society*, **160**, A259 (2013).
5. C. O. Laoire, S. Mukerjee, K. M. Abraham, E. J. Plichta, and M. A. Hendrickson, *The Journal of Physical Chemistry C*, **113**, 20127 (2009).
6. C. O. Laoire, S. Mukerjee, K. M. Abraham, E. J. Plichta, and M. A. Hendrickson, *The Journal of Physical Chemistry C*, **114**, 9178 (2010).
7. A. J. Appleby, in *Comprehensive Treatise of Electrochemistry*, eds. B. Conway, J. M. Bockris, E. Yeager, S. M. Khan, and R. White, Springer US, 1983, ch. 4, pp. 173–239.
8. N. Ramaswamy and S. Mukerjee, *The Journal of Physical Chemistry C*, **115**, 18015 (2011).
9. C. M. A. Dobley, R. Roark, and K. M. Abraham, *proceedings of 42nd Power Sources conference, Philadelphia, PA*, 2006.
10. H. Cheng and K. Scott, *Journal of Power Sources*, **195**, 1370 (2010).
11. L. Wang, X. Zhao, Y. Lu, M. Xu, D. Zhang, R. S. Ruoff, K. J. Stevenson, and J. B. Goodenough, *Journal of The Electrochemical Society*, **158**, A1379 (2011).
12. Y.-C. Lu, Z. Xu, H. A. Gasteiger, S. Chen, K. Hamad-Schifferli, and Y. Shao-Horn, *Journal of the American Chemical Society*, **132**, 12170 (2010).
13. A. Débart, J. Bao, G. Armstrong, and P. G. Bruce, *Journal of Power Sources*, **174**, 1177 (2007).
14. A. Débart, A. J. Paterson, J. Bao, and P. G. Bruce, *Angewandte Chemie International Edition*, **47**, 4521 (2008).
15. Y. Lu, Z. Wen, J. Jin, Y. Cui, M. Wu, and S. Sun, *Journal of Solid State Electrochemistry*, **16**, 1863 (2012).
16. Y.-C. Lu, D. G. Kwabi, K. P. C. Yao, J. R. Harding, J. Zhou, L. Zuin, and Y. Shao-Horn, *Energy & Environmental Science*, **4**, 2999 (2011).
17. J. Chen, J. S. Hummelshøj, K. S. Thygesen, J. S. Myrdal, J. K. Nørskov, and T. Vegge, *Catalysis Today*, **165**, 2 (2011).
18. O. Oloniyo, S. Kumar, and K. Scott, *Journal of Electronic Materials*, **41**, 921 (2012).
19. G. Q. Zhang, J. P. Zheng, R. Liang, C. Zhang, B. Wang, M. Au, M. Hendrickson, and E. J. Plichta, *Journal of The Electrochemical Society*, **158**, A822 (2011).
20. S. Dong, X. Chen, K. Zhang, L. Gu, L. Zhang, X. Zhou, L. Li, Z. Liu, P. Han, H. Xu, J. Yao, C. Zhang, X. Zhang, C. Shang, G. Cui, and L. Chen, *Chemical Communications*, **47**, 11291 (2011).
21. G. Zhang, M. Hendrickson, E. Plichta, M. Au, and J. Zheng, *Journal of The Electrochemical Society*, **159**, A310 (2012).
22. L. Jin, L. Xu, C. Morein, C.-h. Chen, M. Lai, S. Dharmarathna, A. Dobley, and S. L. Suib, *Advanced Functional Materials*, **20**, 3373 (2010).
23. E. Yoo and H. Zhou, *ACS Nano*, **5**, 3020 (2011).
24. T. H. Yoon and Y. J. Park, *Nanoscale research letters*, **7**, 1 (2012).
25. Z. Peng, S. A. Freunberger, Y. Chen, and P. G. Bruce, *Science*, **337**, 563 (2012).
26. Y. Zhao, L. Xu, L. Mai, C. Han, Q. An, X. Xu, X. Liu, and Q. Zhang, *Proceedings of the National Academy of Sciences*, **109**, 19569 (2012).
27. J. Yin, B. Fang, J. Luo, B. Wanjala, D. Mott, R. Loukrakpam, M. S. Ng, Z. Li, J. Hong, and M. S. Whittingham, *Nanotechnology*, **23**, 305404 (2012).
28. W. Yang, J. Salim, C. Ma, Z. Ma, C. Sun, J. Li, L. Chen, and Y. Kim, *Electrochemistry Communications*, **28**, 13 (2013).
29. W. Yang, J. Salim, S. Li, C. Sun, L. Chen, J. B. Goodenough, and Y. Kim, *Journal of Materials Chemistry*, **22**, 18902 (2012).
30. L. Wang, M. Ara, K. Wadumesthrige, S. Salley, and K. Y. S. Ng, *Journal of Power Sources*, **234**, 8 (2013).
31. A. K. Thapa, T. H. Shin, S. Ida, G. U. Sumanasekera, M. K. Sunkara, and T. Ishihara, *Journal of Power Sources*, **220**, 211 (2012).
32. A. K. Thapa, Y. Hidaka, H. Hagiwara, S. Ida, and T. Ishihara, *Journal of The Electrochemical Society*, **158**, A1483 (2011).
33. L. Li and A. Manthiram, *Journal of Materials Chemistry A*, **1**, 5121 (2013).
34. F.-S. Ke, B. C. Solomon, S.-G. Ma, and X.-D. Zhou, *Electrochimica Acta*, **85**, 444 (2012).
35. K.-N. Jung, J.-I. Lee, W. B. Im, S. Yoon, K.-H. Shin, and J.-W. Lee, *Chemical Communications*, **48**, 9406 (2012).
36. H.-G. Jung, Y. S. Jeong, J.-B. Park, Y.-K. Sun, B. Scrosati, and Y. J. Lee, *ACS Nano*, **7**, 3532 (2013).
37. S. S. Zhang, X. Ren, and J. Read, *Electrochimica Acta*, **56**, 4544 (2011).
38. X. Ren, S. S. Zhang, D. T. Tran, and J. Read, *Journal of Materials Chemistry*, **21**, 10118 (2011).
39. M. Ladouceur, G. Lalande, D. Guay, J. Dodelet, L. Dignard-Bailey, M. Trudeau, and R. Schulz, *Journal of The Electrochemical Society*, **140**, 1974 (1993).
40. M. Newville, *Journal of Synchrotron Radiation*, **8**, 322 (2001).
41. V. Gutmann, *Coordination Chemistry Reviews*, **18**, 225 (1976).
42. R. S. Drago, D. C. Ferris, and N. Wong, *Journal of the American Chemical Society*, **112**, 8953 (1990).
43. I. Gunasekara, S. Mukerjee, E. J. Plichta, M. A. Hendrickson, and K. M. Abraham, *Journal of The Electrochemical Society*, **161**, A381 (2014).
44. R. G. Pearson, *Journal of the American Chemical Society*, **85**, 3533 (1963).
45. M. J. Trahan, Q. Jia, S. Mukerjee, E. J. Plichta, M. A. Hendrickson, and K. M. Abraham, *Journal of The Electrochemical Society*, **160**, A1577 (2013).
46. B. Hammer and J. K. Nørskov, in *Advances in Catalysis*, ed. H. K. Bruce and C. Gates, Academic Press, 2000, vol. Volume 45, pp. 71–129.
47. Y. Kessler, Y. Puhovski, M. Kiselev, I. Vaisman, G. Mamantov, and A. Popov, VCH, New York, 1994, 307.
48. C. M. Ó'Laoire, *INVESTIGATIONS OF OXYGEN REDUCTION REACTIONS IN NON-AQUEOUS ELECTROLYTES AND THE LITHIUM-AIR BATTERY, Doctor of Philosophy Dissertation, Northeastern University*, 2010.
49. D. T. Sawyer, G. Chiericato Jr, C. T. Angelis, E. J. Nanni Jr, and T. Tsuchiya, *Analytical Chemistry*, **54**, 1720 (1982).
50. S. S. Zhang, D. Foster, and J. Read, *Journal of Power Sources*, **195**, 1235 (2010).